Sensors & Actuators: B. Chemical 309 (2020) 127772

Contents lists available at ScienceDirect

Sensors and Actuators B: Chemical

journal homepage: www.elsevier.com/locate/snb

Imaging of the mutual regulation between zinc cation and nitrosyl *via* two-photon fluorescent probes in cells and *in vivo*

Mingshun Li[a], Yanlong Xing[b], Yuxia Zou[b], Guang Chen[a,*], Jinmao You[a,*], Fabiao Yu[a,b,*]

[a] The Key Laboratory of Life-Organic Analysis, Key Laboratory of Pharmaceutical Intermediates and Analysis of Natural Medicine, College of Chemistry and Chemical Engineering, Qufu Normal University, Qufu 273165, China

[b] Institute of Functional Materials and Molecular Imaging, Key Laboratory of Emergency and Trauma, Ministry of Education, Key Laboratory of Hainan Trauma and Disaster Rescue, College of Clinical Medicine, College of Emergency and Trauma, Hainan Medical University, Haikou 571199, China

ARTICLE INFO

Keywords:
Fluorescent probes
Two-photon
Zinc cation
Nitrosyl
Cell imaging
In vivo imaging

ABSTRACT

The homeostatic disorder of intracellular Zn^{2+} pool is closely associated with severe diseases. It has been reported that the high level of free Zn^{2+} during ischemia/reperfusion (I/R) process can result in oxidative stress damage on nerve cells. Given that nitrosyl (HNO) can aggravate the nerve injury during cerebral I/R process, we assume that there may exist a mutual regulation between Zn^{2+} and HNO under certain physiological conditions. To reveal this potential small-signaling-molecule crosstalk, we synthesized two-photon fluorescent probes **CHP-H** and **CHP-CH$_3$** to monitor intracellular Zn^{2+} in cell and mice hippocampus I/R models. The probes consist of two moieties: coumarin derivative as the two-photon fluorescence transducer, 2-hydrazino pyridine as the fluorescence modulator and Zn^{2+} chelator. Both probes exhibit excellent analytical properties for Zn^{2+} detection in simulated physiological systems. Utilizing **CHP-H** and an HNO probe **Cyto-JN**, we perform fluorescent imaging of cell I/R models. The results confirm that HNO can stimulate Zn^{2+} release from labile Zn^{2+} pool, whereas, the increase of intracellular Zn^{2+} cannot upregulate the level of HNO. Combining with the deep tissue imaging of mice hippocampus tissues, our probes may provide potential approaches for the medical diagnostic assessment of HNO regulation effect on Zn^{2+} release in clinical cerebral I/R-related diseases.

1. Introduction

As the second extensive transitional metal after iron in organism, zinc cation (Zn^{2+}) plays crucial roles in cells involving intracellular metabolism, apoptosis, enzymatic catalysis, neurotransmission, and so forth [1]. The total concentration range of Zn^{2+} pool in mammalian cells is approximately 100–500 μM, in particular, brain hippocampus is one of the most abundant distribution areas. The most fraction of intracellular Zn^{2+} is tightly chelated in metalloproteins, while the small portion is reserved through complexing with diverse small molecules, such as amino acids, for ready exchangeability. The free Zn^{2+} in cytoplasm has been involved in various signaling pathways that are relevant to different physiological and pathological events. For instance, in hippocampus, the variation in the homeostasis of Zn^{2+} is closely related to severe neurological diseases [2]. Zn^{2+} is involved in cerebral ischemia/reperfusion (I/R) injury and becomes a potentially toxic metal cation in brain. The neurotoxicity mechanism is that the abnormal levels of Zn^{2+} lead to oxidative stress and depolarization in mitochondria, as well as the inhibition of metabolic enzymes activity, and eventually activate apoptosis or necrosis processes in cells. Therefore, the significance of detecting Zn^{2+} is still drawing widespread interests [3].

Reactive nitrogen species (RNS), including nitric oxide (NO), peroxynitrite ($ONOO^-$), and nitrosyl (HNO), are associated with neurological diseases. NO and $ONOO^-$ can not only induce nitrosation of biothiols, but also stimulate the release of Zn^{2+} to trigger a range of zinc-related signal transduction pathway in cells [4,5]. HNO has been considered to be the form of single electron reduction and protonation of NO, which is biologically associated with the cardiovascular and nervous systems. HNO can aggravate the nerve injury during cerebral I/R process *via* oxidative stress. The injury eventually results in severe neurotoxicity and causes irreversible damage in neurons function [6]. Since Zn^{2+} and HNO simultaneously play roles in neuronal oxidative damage, we hypothesize that the intracellular Zn^{2+} may be associated with the intracellular HNO under a certain physiological or pathological state. However, the mutual regulations between Zn^{2+} and HNO

* Corresponding authors at: The Key Laboratory of Life-Organic Analysis, Key Laboratory of Pharmaceutical Intermediates and Analysis of Natural Medicine, College of Chemistry and Chemical Engineering, Qufu Normal University, Qufu 273165, China.

E-mail addresses: chenandguang@163.com (G. Chen), jmyou6304@163.com (J. You), fbyu@yic.ac.cn (F. Yu).

https://doi.org/10.1016/j.snb.2020.127772
Received 19 November 2019; Received in revised form 4 January 2020; Accepted 22 January 2020
Available online 23 January 2020

are still far from clear, which needs to be further investigated [7].

To completely elaborate the roles of intracellular Zn^{2+} in biological events, improved approaches for the selective detection of Zn^{2+} have been well defined. However, most of the detection technologies require tedious sample preparation, time-consuming cell and tissue lysis, and high cost operations. It is challenging for these technologies to realize the real-time and *in situ* tracking of Zn^{2+} in living systems [8]. Therefore, it is extremely urgent to construct advanced chemical tools to meet the requirements of mapping the distribution of intracellular Zn^{2+} [9]. Among the detection technologies, fluorescent bioimaging is considered as a powerful tool for real-time, noninvasive, and *in situ* visualization of Zn^{2+} in living cells. When captures Zn^{2+}, the fluorescent probe switches on its specific fluorescence without damaging cells and provides the detailed information of biological roles of intracellular Zn^{2+}. To date, the available fluorescent probes for intracellular Zn^{2+} detection have been making advanced progress [10]. However, most of these probes whose spectra locate in ultraviolet-visible (UV–vis) range suffer from phototoxicity, intrinsic autofluorescence, and the insufficient penetration depth (less than 100 μm), which limits their normal application to imaging of Zn^{2+} in cells and *in vivo*. To address these issues, two-photon fluorescent probe has been applied in bioimaging due to its unique characteristics in deep tissue penetration, low photodamage to biological samples, weak autofluorescence, as well as high spatial resolution, and is thus favorable for imaging of bio-species in living systems. Although some two-photon probes have been proven to be preferable for imaging of intracellular Zn^{2+} [11–13], in this work, we attempt to reveal the mutual modulations between Zn^{2+} and HNO under a certain physiological state, *e.g.* during I/R process.

Herein, we designed and synthesized two-photon fluorescent probes **CHP-H** and **CHP-CH_3** for the investigation of the crosstalk between Zn^{2+} and HNO in living cells and in hippocampus. Both probes **CHP-H** and **CHP-CH_3** exhibited excellent analytical properties for Zn^{2+} detection including rapid response, high sensitivity, and good selectivity. Another near-infrared (NIR) probe **Cyto-JN** from our previous work was employed for evaluating the changes of intracellular HNO level simultaneously [14]. Owning to their non-overlapping excitation and emission wavelengths, the combined application of **CHP-H** and **Cyto-JN** could maximally eliminate potential interference and efficiently avoid multiple emission overlap between multicolor probes. Utilizing the probes **CHP-H** and **Cyto-JN**, we firstly examined the mutual regulation between intracellular Zn^{2+} and HNO in I/R cell models and in hippocampus tissues. Apoptosis rates were verified *via* flow cytometry analyses which confirmed the biocompatibility of our probes. The above results demonstrated that the endogenous HNO could induce the release of Zn^{2+} from labile Zn^{2+} pool, while the increase of the intracellular level of Zn^{2+} could not upregulate the level of HNO.

2. Experimental

2.1. Synthesis and characterization of probes

2.1.1. Synthesis of Compound 2

The compound 1, 8-hydroxyjulolidine-9-carboxaldehyde (0.504 g, 2.3 mmol) and diethyl malonate (0.736 mL, 4.6 mmol) were dissolved into 20 mL ethanol, then the solution was added 0.23 mL piperidine. The mixed solution was heated and refluxed for 24 h. Subsequently, the mixed system was detected by TLC (thin layer chromatography), and the solvent was removed by vacuum to obtain solid. Subsequently, 8 mL concentrated hydrochloric acid and 8 mL glacial acetic acid were added sequentially to a flask with the solid. Then the three chemicals were stirred to mix and heated to 80 ℃, then reacted for 12 h. After the reaction was accomplished, the solution was cooled to room temperature. Then, the pH value of the solution was adjusted to 7.0 after pouring the solution into 400 mL ice water and adding 20 % NaOH solution. Yellow precipitate slowly appeared in the solution along with stirring for 30 min. Afterwards, the mixture was filtered, washed with pure water, dried in vacuum and recrystallized by toluene to obtain the yellow solid product of Compound 2 (yield: 79.1 %). ^{1}H NMR ($CDCl_3$-d_1, 400 MH_Z) δ (ppm): 7.45–7.43 (d, 1 H), 6.82 (s, 1 H), 5.98–5.96 (d, 1 H), 3.26–3.23 (t, 4 H), 2.88–2.86 (t, 2 H), 2.75–2.73 (t, 2 H), 1.98–1.93 (m, 4 H). ^{13}C NMR ($CDCl_3$-d_1, 125 MH_Z) δ (ppm): 162.79, 151.78, 146.02, 144.06, 125.03, 118.36, 108.48, 108.30, 106.82, 50.07, 49.71, 27.56, 21.58, 20.68, 20.34. HRMS (ESI$^+$): *m/z* $C_{15}H_{15}NO_2$ calcd. 241.1103, found [M + H] $^+$ 242.1175.

2.1.2. Synthesis of Compound 3

The intermediate 10-oxo-2,3,5,6-tetrahydro-1H, 4H, 10H-11-oxa-3a-azabenzo [de] anthracene-9-carbaldehyde (compound 3) was synthesized according to the previously reported method [15]. In brief, phosphorus oxychloride ($POCl_3$) was added dropwise to 2.0 mL of anhydrous DMF and the mixture was stirred for 30 min at room temperature under a nitrogen atmosphere. The reaction solution gradually turned light-yellow while stirring. Compound 3 was dissolved in 3 mL anhydrous DMF, and the solution was added to the above light-yellow solution. The mixture was stirred at room temperature for 30 min then heated to 60 ˚C to allow the reaction for 12 h. After the reaction was completed, the solution was slowly poured into 100 mL of ice water. Then the pH of the solution was adjusted to 7.0 by adding 20 % NaOH solution. The precipitate appeared in the solution, and the solid was obtained by filtration. Then the product was recrystallized by absolute ethanol to offer the Compound 3 (yield: 62.3 %).^{1}H NMR ($CDCl_3$-d_1, 400 MH_Z) δ (ppm): 10.10 (s, 1 H), 8.13 (s, 1 H), 6.97 (s, 1 H), 3.36–3.34 (t, 4 H), 2.89–2.86 (t, 2 H), 2.76–2.74 (t, 2 H), 1.98–1.96 (m, 4 H). ^{13}C NMR ($CDCl_3$-d_1, 125 MH_Z) δ (ppm): 188.23, 162.46, 153.97, 149.47, 145.21, 128.46, 119.97, 113.18, 108.26, 106.31, 50.54, 50.14, 27.44, 21.11, 20.15, 20.11. HRMS (ESI$^+$): *m/z* $C_{16}H_{15}NO_3$ calcd. 269.1052, found [M + H] $^+$ 270.1126.

2.1.3. Synthesis of CHP-H

The intermediate 3 (0.269 g, 1.0 mmol) and 2-hydrazino pyridine (0.164 g, 1.5 mmol) were dissolved in 20 mL anhydrous ethanol. Then three drops of glacial acetic acid were added to the solution which was heated slowly to reflux for 4 h and monitored using TLC (thin layer chromatography). After the reaction was accomplished, the solution was cooled to room temperature, with red precipitate appeared. The mixture was filtered and the red solid was obtained as **CHP-H** (yield, 76 %). ^{1}H NMR (d_6-DMSO, 400 MH_Z) δ (ppm): 10.92 (s, 1 H), 8.19 (s, 1 H), 8.10–8.08 (d, 1 H), 8.05 (s, 1 H), 7.63–7.60 (t, 1 H), 7.26 (d, 1 H), 7.17 (s, 1 H), 6.78–6.73 (m, 1 H), 3.30–3.27 (t, 4 H), 2.75–2.71 (t, 4 H), 1.93-1.85 (m, 4 H). ^{13}C NMR (d_6-DMSO, 125 MH_Z) δ (ppm): 171.11, 161.41, 157.39, 151.21, 148.22, 146.46, 138.24, 136.69, 133.97, 126.40, 119.19, 115.32, 113.57, 108.61, 106.81, 105.81, 49.87, 49.36, 27.36, 21.30, 20.40. HRMS (ESI$^+$): *m/z* $C_{21}H_{21}N_4O_2^+$ calcd. 361.1659, found [M + H] $^+$ 361.1666.

2.1.4. Synthesis of Compound 4

The compound 1, 8-hydroxyjulolidine-9-carboxaldehyde, (0.650 g, 3 mmol) and ethyl acetoacetate (1.0 mL, 7.5 mmol) were dissolved into 24 mL ethanol, then the solution was added 0.50 mL piperidine. The mixed solution was heated and refluxed for 6 h. After the reaction was accomplished, the mixed solution was cooled to room temperature then filtrated to obtain orange crystals. The crystals were washed by cold ethanol and dried in vacuum to offer the desired product Compound 4. (yield: 75.3 %). ^{1}H NMR (400 MHz, $CDCl_3$-d_1) δ (ppm): 8.31 (s, 1 H), 6.94 (s, 1 H), 3.33–3.30 (t, 4 H), 2.86–2.84 (t, 2 H), 2.76–2.74 (t, 2 H), 2.64 (s, 3 H), 1.97–1.93 (m, 4 H). ^{13}C NMR ($CDCl_3$-d_1, 125 MH_Z) δ (ppm): 196.08, 161.33, 153.85, 148.82, 147.87, 127.84, 119.60, 114.96, 108.13, 105.70, 50.01, 30.70, 27.49, 21.20, 20.12. HRMS (ESI$^+$): *m/z* $C_{17}H_{17}NO_3$ calcd. 283.1028, found [M + H] $^+$ 284.1280.

2.1.5. Synthesis of CHP-CH_3

The intermediate 4 (Scheme 1) (0.285 g, 1 mmol) and 2-hydrazino

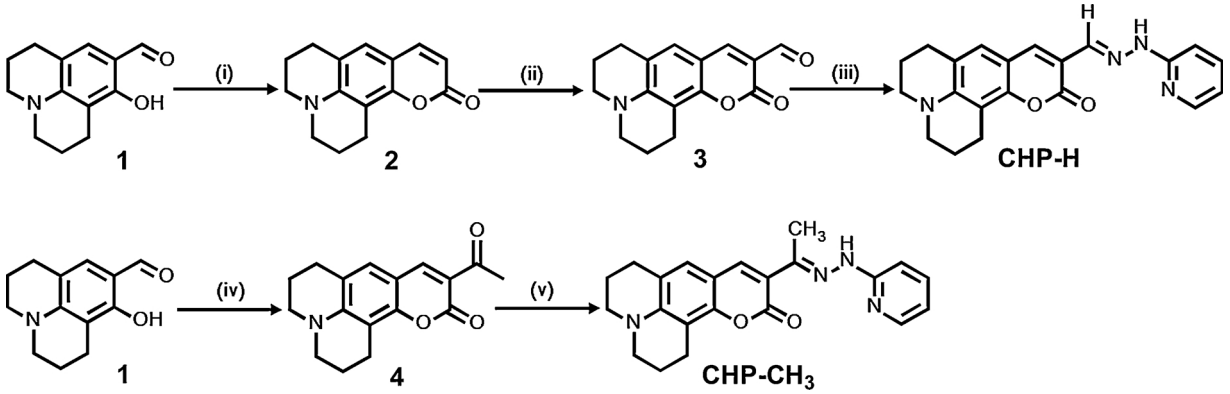

Scheme 1. The procedures for the syntheses of probes CHP-H and CHP-CH_3. (i) 8-hydroxyjulolidine-9-carboxaldehyde, diethyl malonate, piperidine and ethanol; reflux. HCl (con.), acetic acid; heat and stir. (ii) DMF, $POCl_3$; stir. (iii) 2-hydrazinopyridine, ethanol; reflux. (iv) ethyl acetoacetate, piperidine, ethanol; reflux. (v) 2-hydrazinopyridine, ethanol; reflux.

pyridine (0.164 g, 1.5 mmol) were dissolved in 20 mL anhydrous alcohol. The mixed solution was heated slowly to 80 ˚C. After reflowing for 10 h, the reaction solution was cooled to room temperature and the light-yellow precipitate slowly emerged. The mixture was filtered to obtain the precipitated product. Then the crude product was purified by column chromatography (eluent petroleum ether/ethyl acetate = 5/1 v/v) to yield light-yellow needle crystals as **CHP-CH_3** (41 %). ^{1}H NMR (400 MHz, $CDCl_3$-d_1) δ (ppm): 10.90 (s, 1 H), 8.12–8.11 (d, 1 H), 7.76 (s, 1 H), 7.60–7.56 (t, 1 H), 7.04–7.02 (d, 1 H), 6.76-6.73 (m, 1 H), 6.60 (s, 1 H), 3.20–3.17 (t, 4 H), 2.76–2.69 (m, 4 H), 1.99–1.95 (t, 4 H), 1.93 (s, 3 H). ^{13}C NMR ($CDCl_3$-d_1, 125 MHz) δ (ppm): 161.18, 155.40, 150.02, 149.23, 144.35, 142.35, 138.50, 137.89, 131.74, 123.20, 122.06, 120.26, 117.98, 110.35, 109.08, 106.50, 49.06, 46.48, 26.81, 23.29, 21.19, 12.57. HRMS (ESI$^+$): *m/z* $C_{22}H_{23}N_4O_2^+$ calcd. 375.1816, found $[M+H]^+$ 375.1818.

2.2. Construction of cell I/R models

2.2.1. Glucose-serum-oxygen deprivation/reperfusion model

The glucose-serum-oxygen deprivation/reperfusion model was constructed to simulate the I/R state in living mice neuron cell line (HT22 cells) [16]. The HT22 cells were cultivated in glucose and serum free DMEM (dulbecco's modified eagle medium) and placed in an anaerobic chamber (Billups Rothenberg) at 37 ˚C including 95 % N_2 and 5 % CO_2. HT22 cells were cultivated under the condition for 2 h as glucose-serum-oxygen deprivation. Then the waste medium was substituted with fresh DMEM with high glucose and serum content and then exposed to a humidified atmosphere containing 5 % CO_2. The cells were served as reperfusion at 37 ˚C inducing I/R injury.

2.2.2. Glucose deprivation/reperfusion model

HT22 cells were incubated under glucose-free DMEM containing 10 % serum in a humidified atmosphere of 5 % CO_2 at 37 ˚C for 2 h as glucose deprivation. Then HT22 cells were cultured in DMEM medium containing high glucose at 37 ℃ as a glucose deprivation/reperfusion model.

2.2.3. Serum deprivation/reperfusion model

HT22 cells were incubated in serum free DMEM including high glucose in a humidified atmosphere of 5 % CO_2 at 37 ˚C for 2 h as serum deprivation. Then HT22 cells were exposed to DMEM medium containing serum and high glucose at 37 ℃ as a serum deprivation/reperfusion model.

2.2.4. Oxygen deprivation/reperfusion model

HT22 cells were cultured in DMEM involving glucose and serum and placed in an anaerobic chamber filling a mixed gas of 5 % CO_2 and 95 % N_2 at 37 ˚C for 2 h as oxygen deprivation. Then HT22 cells were cultured in DMEM containing glucose and serum, which was exposed to a humidified atmosphere including 5 % CO_2 at 37 ℃ as an oxygen deprivation/reperfusion model.

2.3. Establishment of hippocampus I/R model

The cerebral I/R model was similar to previously reported description [17]. In brief, mice from Hainan Medical University were anesthetized with isoflurane. Midline incision was operated in mouse neck and the left common and external carotid artery were separated and ligated (5–0 silk). A silk thread (6-0 nylon, blunted 0.22–0.24 mm) was inserted into the external carotid artery and forwarded into the middle cerebral artery until slight resistance was felt (sketchily 9 mm) for 1 h. At the same time, the posterior cerebral artery was ligated through the vertebral artery pathway and blocked for 1 h. The thread was removed, and blood flow returned to normal for 2 h. The brain I/R model was established. Mice acute decapitation were performed and hippocampus was separated. Coronal and sagittal slices were skived into thickness 100 μm in ice cold oxygenated artificial cerebrospinal fluid (ACSF) using vibration slicer. The Ethics Committee of Hainan Medical University approved this study. All surgical procedures and experimental protocols were approved by the Institutional Animal Care and Use Committee in Hainan Medical University, Haikou, China.

3. Results and discussion

3.1. Design strategy of two-photon probes for Zn^{2+} detection

To conceive a desirable fluorescent probe for the selective detection of Zn^{2+} in biological systems, we inspect the design strategies. A reliable Zn^{2+} fluorescent probe commonly features as: excellent chemical and photostability, good fluorescence selectivity and sensitivity, rapid response time, suitable membrane permeability, as well as adequate biocompatibility [18–20]. In order to achieve the goal of Zn^{2+} detection in a complex biological system, the probe that exhibits two-photon excitation wavelength is more favorable to biological experiments which require real-time, *in situ*, and prolonged observation. In addition, the Zn^{2+} probe must meet the requirements of multicolor bioimaging of multianalytes when combining with other probes [21–27]. Bearing these principles in mind, we make efforts to design new Zn^{2+} probes to meet the urgent requirement.

We pick out a 7-aminocoumarins' derivative as the design fluorophore platform, which possesses high fluorescent quantum yield, excellent biocompatibility, strong and stable fluorescence emission, and good structural flexibility [28]. In particular, the two-photon characteristic of the coumarin-based fluorophore can effectively avoid

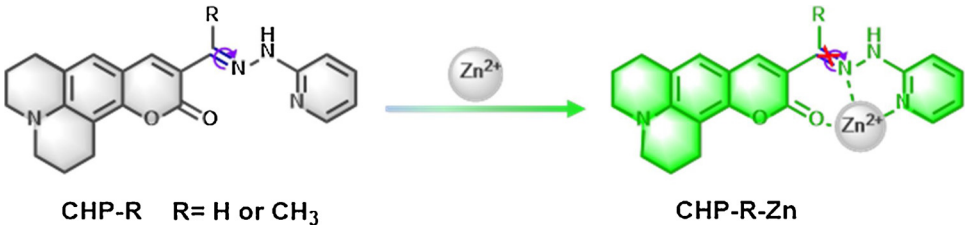

Scheme 2. The molecule structure of probes and proposed detection mechanism against Zn^{2+}.

spectral overlap interference in multicolor imaging. Apart from the choice of a suitable fluorophore platform, the modification of chelating moiety for specially trapping Zn^{2+} is critical for the probe. A preferential chelating ligand should have a dissociation constant (K_d) that possesses the similar order of magnitude as the concentration of the free metal ion in cells. If the chelator's binding affinity is too strong, it may remove the ion from storage proteins or enzymes, which will obstruct the metal ion's intracellular homeostasis. Conversely, a chelator which has a weak binding affinity cannot trap the available metal ion of interest [29]. It has been verified that the intracellular level of Zn^{2+} in hippocampal CA1 area transiently increases and reaches a maximum of ~nM level [17]. Based on this concentration change, we optimize the synthesis procedure and obtain a Schiff base chelator for Zn^{2+} detection, due to the appropriate affinity of the nitrogen of the Schiff base for Zn^{2+} [10,30–32]. Two fluorescent probes **CHP-H** and **CHP-CH_3** were obtained by conjugating two-photon coumarin fluorophores and 2-hydrazinepyridine. The syntheses of the probes could be found in the experimental section (Scheme 1).

As illustrated in Scheme 2, the detection photophysical mechanism was proposed to be as the isomerization and rotation of C=N, which could strengthen the decay process of the excited states for fluorophore resulting in quenching of the fluorescence emission of the probes [33]. However, once binding by Zn^{2+}, the isomerization and rotation of the C=N group would be dramatically obstructed, resulting in an obvious recovery of fluorescence. To verify the proposed mechanisms of our probes, we utilized the viscosity assay to hinder the isomerization and rotation of C=N [34–37]. As shown in Figs. S1 and S2, both probes were initially non-fluorescent in low viscosity solvent, while exhibited gradual enhanced fluorescence with the increasing of viscosity. The result elucidated that the low-viscosity solvent failed to block the isomerization and rotation of C=N, which quenched the fluorescence of the probes. However, when the energy decay process was restrained by the solvent's viscosity, there would be strong fluorescence signal. Moreover, the NIR excitation of the two-photon fluorescent profiles behaved no spectral overlap with that of HNO probe **Cyto-JN**, which contributes to multicolor imaging.

3.2. Spectroscopic properties and selectivity of probes

The spectroscopic properties of the two probes **CHP-H** and **CHP-CH_3** were examined under simulated physiological condition (pH 7.4, 10 mM HEPES buffer solution). As indicated in Fig. 1a, the probe **CHP-H** displayed an absorption band with the maximum peak at ~490 nm after chelated with Zn^{2+}. The probe **CHP-CH_3** exhibited an absorption band peaked at 370 nm, with an obvious bathochromic shift from 370 to 405 nm when detected Zn^{2+} (Fig. S3a). The difference in the absorption of the two probes could be attributed to the stronger electron donating capability of methyl substituent in **CHP-CH_3** than that of hydrogen atom in **CHP-H** [38]. Accompanied by the restriction of the isomerization and rotation of C=N upon Zn-chelating, both probes triggered the switch-on fluorescence and large Stokes shifts of approx. 100 nm in the fluorescence emission spectra (Figs. 1b and S3b). In the presence of increasing concentration of Zn^{2+} (0.0–1.0 μM), the fluorescence intensity ratio ΔF of **CHP-H** (1.0 μM) displayed a large enhancement of ~ 7-fold at emission wavelength 543 nm (Fig. 1b), whereas the ΔF of **CHP-CH_3** (1.0 μM) increased only ~ 4 folds (λ_{em} = 523 nm) (Fig. S3b). The linear response between ΔF of the two probes and the concentration of Zn^{2+} were obtained (Figs. 1c and S3c), with the linear regression equations for the probe **CHP-H** to be ΔF = 6.7678 [Zn^{2+}] – 0.2131 (r = 0.9983) and that for the probe **CHP-CH_3** was ΔF = 3.4619 [Zn^{2+}] + 0.4079 (r = 0.9975). The limits of detection ($3\sigma/k$) were calculated to be 19 nM and 25 nM for **CHP-H** and **CHP-CH_3**, respectively, in which σ was the standard deviation of blank sample detection and k was slope of the linear regression equation. Both probes exhibited high photostability (Figs. S4 and S5) and 1:1 stoichiometry with Zn^{2+} through the equimolar continuous-variation plots (Figs. S6 and S7) [39]. The reaction mechanism of both probes and Zn^{2+} were verified by NMR titration and high-resolution mass spectrometry (HRMS) (Figs. S8 and S9). The dissociation constants (K_d) of the probes **CHP-H** and **CHP-CH_3** for complexing Zn^{2+} were determined to be 3 nM and 12 nM, respectively, calculated from the Benesi-Hildebrand plots (Figs. S10 and S11) [40]. The above results implied that the proposed probes were suitable for detecting intracellular changes of Zn^{2+} level, because their dissociation constants (K_d) were at the similar order of magnitude as the concentration of the free Zn^{2+} in cells. After the detection of Zn^{2+}, the fluorescence quantum yields of the probes were calculated to be 0.50 and 0.29, respectively. The δ_{max} of **CHP-H-Zn** and **CHP-CH_3-Zn** were 121 GM and 51 GM (Goeppert-Mayer) at an excitation wavelength of 880 and 900 nm (Figs. S12 and S13) [41]. Therefore, our probes possessed good two-photon properties and enabled apparently strong fluorescence enhancement after reaction due to nearly completely quenched fluorescence in the absence of the Zn^{2+}.

Although pH values were strictly restricted in a range of 7.4 ± 0.05 unit under physiological conditions, the pH dependent fluorescence should be avoided for the further application in complex biological systems. Following, we tested the pH effects of buffer solutions on the fluorescence emission under diverse pH values. As illustrated in Figs. 1d and S3d, both probes offered no response under pH range from 0.0 to 9.0 owing to the quenched fluorescence emission by the C=N isomerization and rotation of C=N group. When chelating Zn^{2+}, the isomerization and rotation was dramatically obstructed, therefore, the two probes provided increased fluorescence emissions and were relatively stable in physiological pH range. Therefore, both **CHP-H** and **CHP-CH_3** possessed potential capabilities of bioimaging of Zn^{2+} under physiological conditions. We next examined the reaction kinetics of the probes toward Zn^{2+}. **CHP-H** and **CHP-CH_3** were firstly maintained for 20 s in the testing system. Upon subsequently adding a dose of Zn^{2+}, both probes displayed gradual increase of fluorescence response, and plateaued after another 60 s and 70 s, respectively (Figs. 1e and S3e), which implied the rapid detection of Zn^{2+} with our probes. The interference from other bioreactive species in complex biosystems should be considered. The selectivity of **CHP-H** and **CHP-CH_3** against other interfering metal cations was investigated by using various concentrations of cations in organisms including: Na^+ (10 mM), K^+ (140 mM), Mg^{2+} (0.5 mM), Ca^{2+} (100 μM), Co^{2+} (10 μM), Cu^{2+} (10 μM), Ni^{2+} (10 μM), Mn^{2+} (10 μM), Fe^{2+} (10 μM), Pb^{2+} (10 μM), Hg^{2+} (10 μM), Ba^{2+} (10 μM), Cd^{2+} (10 μM) and Al^{3+} (10 μM). The selectivity of **CHP-H** and **CHP-CH_3** was also examined in the presence of various anions, biothiols, reactive sulfur species (RSS), reactive oxygen species (ROS), and reactive nitrogen species (RNS). As shown in Figs. 1f and S14 (**CHP-H**), S3f and S15 (**CHP-CH_3**), our probes featured high specificity and selectivity toward Zn^{2+} under physiological condition. The above

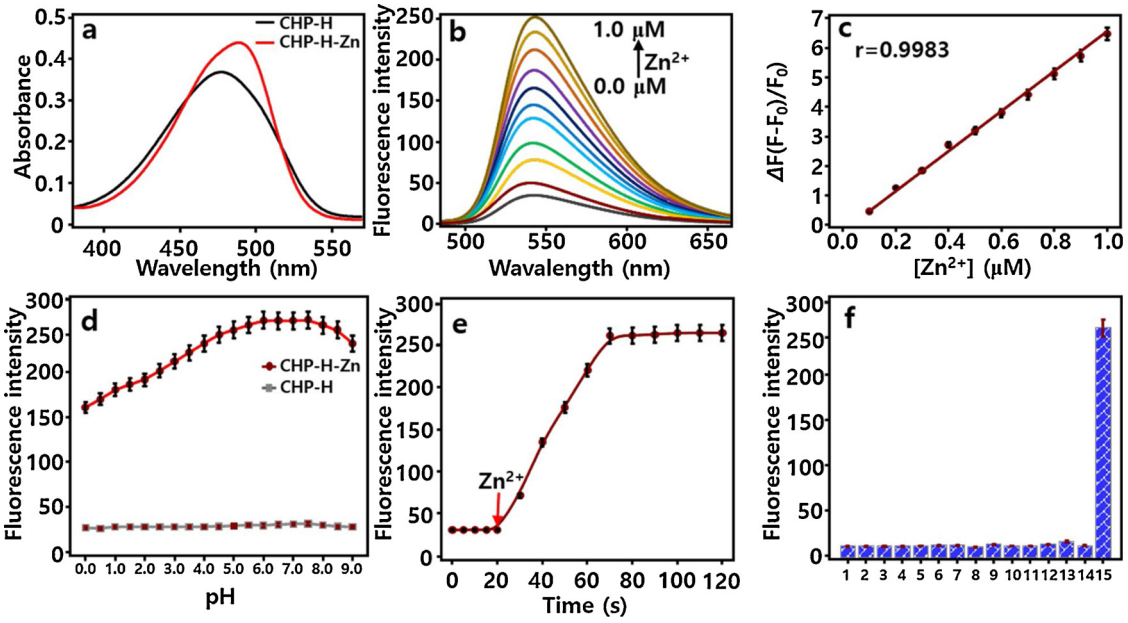

Fig. 1. Spectroscopic properties and selectivity of probe **CHP-H**. **CHP-H** (1.0 μM) mixed with various concentrations of Zn^{2+} (0.0–1.0 μM) at 37 °C in HEPES (pH 7.4, 10 mM) for 3 min ($\lambda_{ex}/\lambda_{em}$ = 465/543 nm). a) Absorbance of **CHP-H** (1.0 μM) in absent (black) and present (red) of Zn^{2+} (1.0 μM). b) Fluorescence titration of **CHP-H** (1.0 μM) with increasing concentrations of Zn^{2+}: 0.0, 0.1, 0.2, 0.3, 0.4, 0.5, 0.6, 0.7, 0.8, 0.9, and 1.0 μM. c) The linear relationship between the fluorescent intensity ratio $\Delta F = (F\text{-}F_0)/F_0$ and Zn^{2+} levels. d) The fluorescence emission changes of **CHP-H** at 543 nm toward the pH range of 0.0–9.0 in the absent and present of Zn^{2+} (1.0 μM). e) Fluorescence intensities of **CHP-H** (1.0 μM) against the reaction time in the presence of Zn^{2+} (1.0 μM). f) Selectivity of **CHP-H** (1.0 μM) in the presence of various metal ions: 1. Na^+ (10 mM), 2. K^+ (140 mM), 3. Mg^{2+} (0.5 mM), 4. Ca^{2+} (100 μM), 5. Co^{2+} (10 μM), 6. Cu^{2+} (10 μM), 7. Ni^{2+} (10 μM), 8. Mn^{2+} (10 μM), 9. Fe^{2+} (10 μM), 10. Pb^{2+} (10 μM), 11. Hg^{2+} (10 μM), 12. Ba^{2+} (10 μM), 13. Cd^{2+} (10 μM), 14. Al^{3+} (10 μM), 15. Zn^{2+} (1.0 μM). The experiments were repeated three times and the data were shown as mean (± s.d.). (For interpretation of the references to colour in this figure legend, the reader is referred to the web version of this article.)

results clearly illustrated that both **CHP-H** and **CHP-CH$_3$** could rapidly and selectively respond to Zn^{2+} with high sensitivity, with **CHP-H** exhibited even better spectral characteristics than **CHP-CH$_3$**.

3.3. Imaging of Zn^{2+} in living cells

To further validate the potential of our probes in visualizing intracellular Zn^{2+}, bioimaging experiments need to be performed. Prior to imaging, the cytotoxicity of **CHP-H** and **CHP-CH$_3$** were tested *via* the Cell Counting Kit - 8 assay. The high cell survival rate displayed in Figs. S16 and S17 proved the low cytotoxicity of our probes to living cells, while **CHP-H** possessed even better biocompatibility than **CHP-CH$_3$**. Additionally, considering the superior analytical characteristics of **CHP-H** to **CHP-CH$_3$**, the probe **CHP-H** was chosen to further study the real-time and *in situ* fluorescence imaging of Zn^{2+} in cells, tissues and mice models. For the simultaneous detection of HNO, our previous HNO probe **Cyto-JN** was exploited because the two probes showed no overlap in their spectra and thus are favorable to multicolor imaging [41]. Three types of cell lines including hepatoblastoma cell line (HepG2 cells), human gastric cancer cell line (SGC-7901 cells) and non-small cell lung cancer cell line (A549 cells) were employed for testing the imaging capability of the probe **CHP-H** for Zn^{2+} detection in two-photon confocal fluorescent imaging experiments. The three cell lines shown in Fig. 2a were pretreated with 25 μM zinc gluconate and 1 mM Angeli's Salt (a commercial HNO donor) for 30 min. After washed three times by fresh cell culture medium, the testing cells were further incubated with 1 μM **CHP-H** for 5 min, 5 μM **Cyto-JN** for 15 min, and 100 ng/mL DAPI (a nuclear dye) for 30 min, respectively. Fluorescence signals were collected in three different emission windows for **CHP-H** (green channel, λ_{ex} =880 nm, λ_{em} = 520–580 nm), **Cyto-JN** (red channel, λ_{ex} =680 nm, λ_{em} = 690–720 nm), and **DAPI** (blue channel, λ_{ex} =405 nm, λ_{em} = 420–480 nm). As shown in Fig. 2a, the cellular fluorescence signals in red and green channels were apparently strong, which suggested the efficient simultaneous detection of HNO and Zn^{2+} by **Cyto-JN** and **CHP-H**, respectively. Comparison of the fluorescence imaging of the three channels and merged outcomes could suggest the cytoplasmic location of the probe **CHP-H**. Furthermore, flow cytometry analyses in Fig. 2b demonstrated that the fluorescence intensities of the probes **CHP-H** and **Cyto-JN** were well consistent with the bioimaging results in red and green channels in Fig. 2a. Thus, **CHP-H** not only featured favorable properties of Zn^{2+} detection in various living cells, but also exhibited promising capability of examining the relationship between Zn^{2+} and HNO in combination with HNO probe **Cyto-JN**.

3.4. Evaluation of the mutual regulations between Zn^{2+} and HNO in living cells

Following, we intended to verify the mutual modulations between Zn^{2+} and HNO in cells. The neuron cell line (HT22 cells) was selected as the testing model. Here, the developed probe **CHP-H** was employed to monitor the concentration fluctuations of endogenous Zn^{2+} under the regulation of HNO (generated from Angeli's Salt), while the changes of endogenous HNO modulated with exogenous Zn^{2+} was examined by the HNO probe **Cyto-JN**. The testing cells in Fig. 3a were divided into three groups: the control group, HNO stimulation group, and Zn^{2+} stimulation group. Initially, the HNO-stimulation group was treated with 1 mM Angeli's Salt for 3 h and the Zn^{2+}-stimulation group was pretreated with Zn^{2+} (25 μM zinc gluconate) for 3 h. After washed three times by fresh cell culture medium, all the cells in the three groups were incubated with 1 μM **CHP-H** for 5 min and 5 μM **Cyto-JN** for 15 min. As shown in the control group of Fig. 3a, HT22 cells gave invisible fluorescence along the time from 0 to 60 min in both red and green channels, indicating nearly no intracellular HNO and free Zn^{2+} to be detected under normal condition. In the HNO-stimulation group, the probe **Cyto-JN** provided apparent red fluorescence which represented the high level of HNO in cells. Under the modulation of HNO, the cells

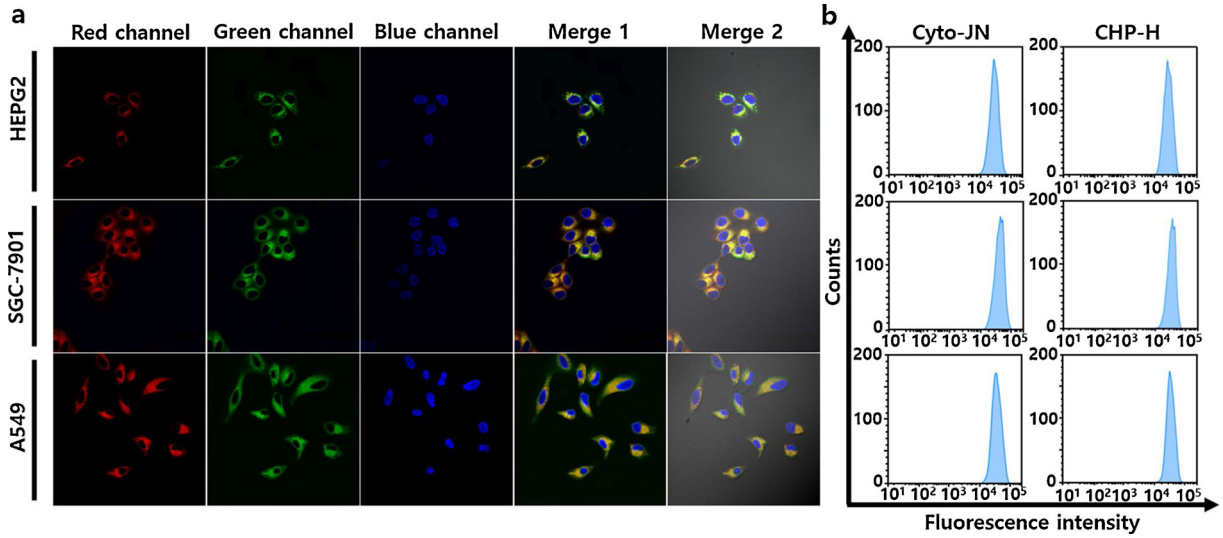

Fig. 2. Imaging capability of the probe **CHP-H** for Zn^{2+} detection in living hepatoblastoma cell lines (HepG2 cells), human gastric cancer cell lines (SGC-7901 cells) and non-small cell lung cancer cell lines (A549 cells). a) Three types of cell lines were pretreated with 1 mM Angeli's Salt (an HNO donor) and 25 μM zinc gluconate for 30 min, respectively, and subsequently incubated with 1 μM **CHP-H** for 5 min, 5 μM **Cyto-JN** (HNO probe) for 15 min, and 100 ng/mL DAPI with for 30 min. Scale bars: 20 μm. b) Flow cytometry analyses of red and green channel in a). Fluorescence collection windows: λ_{ex} = 880 nm, λ_{em} = 520–560 nm (**CHP-H** green channel); λ_{ex} = 680 nm, λ_{em} = 690–720 nm (**Cyto-JN** Red channel); λ_{ex} = 405 nm, λ_{em} = 420 − 480 nm (DAPI blue channel). (For interpretation of the references to colour in this figure legend, the reader is referred to the web version of this article.)

labelled with the probe **CHP-H** exhibited gradual increase of green fluorescence with the extension of time in 60 min, implying the increasing level of intracellular Zn^{2+}. These results confirmed that the increase of intracellular HNO could induce the release of free Zn^{2+} from Zn^{2+} pool in cells. However, as displayed in the Zn^{2+} stimulation group, exogenous Zn^{2+} could not induce any change of fluorescence in red channel during the time range from 0 to 60 min, which demonstrated that even high level of exogenous Zn^{2+} (25 μM) could not trigger the generation of intracellular HNO. The mean intensities in Fig. 3b were quantitative evaluation of the imaging results in Fig. 3a, providing direct insight into the fluorescent changes in the three different groups of living cells. The flow cytometry analyses in Fig. 3c and d were highly consistent with the bioimaging outcomes in Fig. 3a, which further proved the efficacy in using multicolor confocal microscopy images of **CHP-H** and **Cyto-JN** to investigate the intracellular interaction between Zn^{2+} and HNO. The above results demonstrated

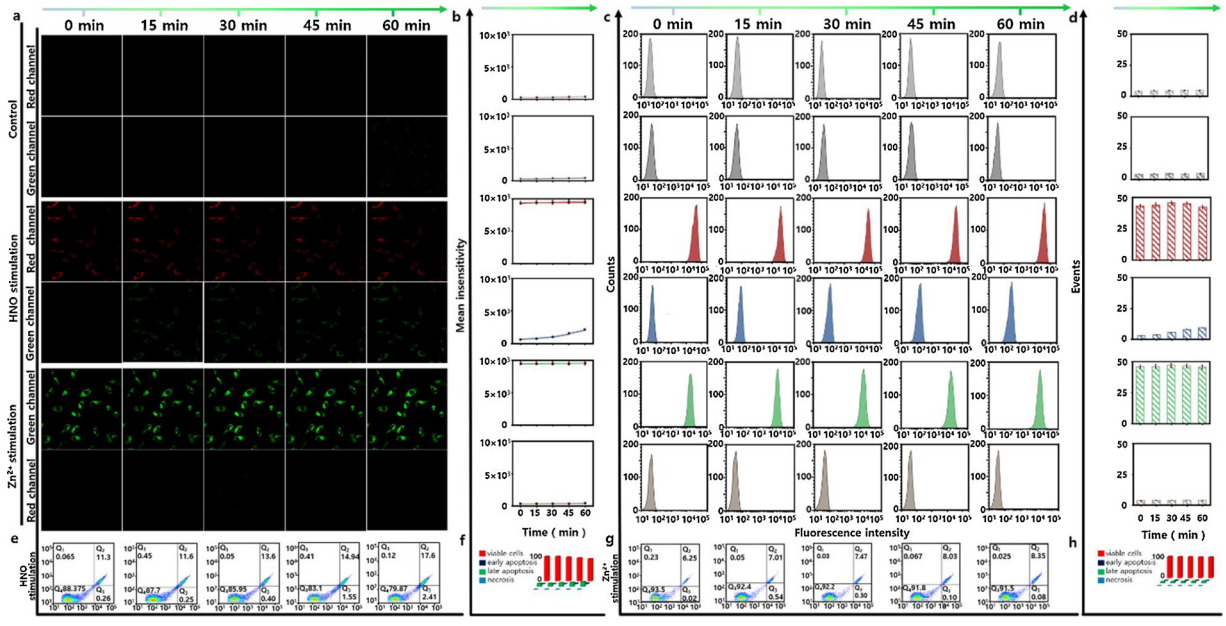

Fig. 3. Confocal microscopy images and flow cytometry assay for evaluating the mutual regulations between Zn^{2+} and HNO in HT22 cells. a) All cells were treated with **CHP-H** (1 μM) for 5 min and **Cyto-JN** (5 μM) for 15 min, then the cells were washed, and the images were acquired at different time points: 0, 15, 30, 45, 60 min. The HNO-stimulation group: the HT22 cells were incubated with Angeli's Salt (1 mM) for 3 h. The Zn^{2+}-stimulation group: the HT22 cells were incubated with Zn^{2+} (25 μM) for 3 h. Fluorescence collection windows: λ_{ex} = 880 nm, λ_{em} = 520–560 nm (**CHP-H** green channel). λ_{ex} = 680 nm, λ_{em} = 690–720 nm (**Cyto-JN** red channel). Scale bars: 20 μm. b) The corresponding mean intensity changes of fluorescence images in a). c) Flow cytometry analyses for a). d) Mean values of c). e) Apoptosis analysis detected by Annexin V-FITC assay for HNO-stimulation group. f) The apoptosis ratio in e). g) Apoptosis analysis by Annexin V-FITC for Zn^{2+}-stimulation group. h) The percentage of apoptosis in g). Q_1: necrosis cells, Q_2: late apoptotic cells, Q_3: early apoptotic cells, Q_4: survival cells. The data were shown as mean (± s.d.). (For interpretation of the references to colour in this figure legend, the reader is referred to the web version of this article.)

that the mutual regulations between Zn^{2+} and HNO in living cells was unidirectional. That was, the increase of the level of HNO would promote the release of Zn^{2+} from intracellular Zn^{2+} pool, however, the increase of intracellular free Zn^{2+} could not modulate the generation of HNO.

We also evaluated and analyzed apoptosis utilizing Annexin V/FITC Apoptosis Detection Kit at different time points of 0 min, 15 min, 30 min, 45 min, and 60 min. As illustrated in Fig. 3e and f, the apoptosis rates of HNO stimulating group were determined to be (11.56 %, Q_2 + Q_3), (11.85 %, Q_2 + Q_3), (14.00 %, Q_2 + Q_3), (16.49 %, Q_2 + Q_3) and (20.01 %, Q_2 + Q_3), which exhibited a gradually increasing trend of apoptosis over the time from 0 to 60 min. That meant, the excessive dose of HNO could induce apoptosis. In the Zn^{2+} stimulation group (Fig. 3g and h), the apoptosis rates were (6.27 %, Q_2 + Q_3), (7.55 %, Q_2 + Q_3), (7.77 %, Q_2 + Q_3), (8.13 %, Q_2 + Q_3), (8.43 %, Q_2 + Q_3), which was lower than those of HNO-stimulation group but higher than the control group (3.53 %, Q_2 + Q_3; 3.89 %, Q_2 + Q_3; 4.046 %, Q_2 + Q_3; 3.90 %, Q_2 + Q_3; 4.67 %, Q_2 + Q_3; Fig. S18). This could be explained as following: when exposed to a high concentration of Zn^{2+}, the cells would initially activate the zinc-buffering reaction system against the intracellular Zn^{2+} pool homeostasis, which helped mitigate the apoptosis [42]. The order of apoptosis rate was sorted as HNO-stimulation group > Zn^{2+}-stimulation group > the control group. Taken together, the intracellular HNO could trigger the release of Zn^{2+} accompanied by the occurrence of apoptosis, while no severe apoptosis induced by the free Zn^{2+}.

3.5. Imaging of HNO-regulated Zn^{2+} release during I/R process

After validating the efficacious modulation of Zn^{2+} release by HNO in living cells, the probe was further employed to verify the concentration fluctuations of Zn^{2+} induced by HNO during cell I/R process. The assays were designed to imitate the cellular I/R process under HNO-stimulation by changing the culture conditions. The HT22 cells were set as: group a, glucose deprivation; group b, serum deprivation; group c, oxygen deprivation; group d, glucose-serum-oxygen deprivation. Different groups of cells were firstly treated by the separate deprivation process for 30 min. Subsequently, all the deprivation manipulations were restored to normal culture conditions with reperfusion time points at 45 and 60 min. The control group was treated in the same manner as described in group d but without HNO-stimulation. Before the operation of deprivation/reperfusion, all the HT22 cells were pretreated with 1 μM **CHP-H** for 5 min, then the cells were washed with fresh cell culture medium for three times to remove the surplus probe from cell culture system. Afterwards, 1 mM Angeli's Salt was added into Petri dishes. The confocal images in Fig. 4a were collected at the time points of 0, 15, 30, 45, and 60 min from the five groups, respectively. The control group displayed nearly no fluorescence changes, implying the tiny fluctuations of endogenous free Zn^{2+} in HT22 cells during glucose-serum-oxygen deprivation/reperfusion process. By contrast, the fluorescence intensity sharply enhanced after 30 min in group d, which evidenced the outburst of endogenous free Zn^{2+} in cytoplasm after the stimulation of HNO. Group b with serum deprivation and group c with oxygen deprivation offered almost the same level of Zn^{2+} release after 30 min, while group a with glucose deprivation resulted in a small amplitude fluctuation of Zn^{2+} during the HNO-stimulation. The mean fluorescence intensity in Fig. 4b illustrated the quantitative results of Fig. 4a. The different fluorescence intensities were related to the distinct levels of Zn^{2+}-burst induced by HNO-stimulation during the diverse I/R cell models. The degree of regulation was arranged in an order of group d > group c > group b > group a > control. We also performed flow cytometry analyses to further confirm the results. As illustrated in Fig. 4c and d, the results were completely consistent with the fluorescence images in Fig. 4a. The above results demonstrated that the probe **CHP-H** behaved a potential ability to serve as a chemical tool for tracing the endogenous free Zn^{2+} outburst during I/R cell models under HNO stimulation.

3.6. Evaluation of the Zn^{2+}/HNO crosstalk in mice hippocampus I/R models

Hippocampus of the brain takes the responsibility of memory and learning, where Zn^{2+} is abundant and indispensable. The variation of Zn^{2+} homeostasis will lead to severe neurological diseases [33,43]. Therefore, the mutual regulatory effects between Zn^{2+} and HNO in mice hippocampus during I/R process is highly desired to be clarified. Moreover, the two-photon fluorescent profiles based NIR excitation can minimize photodamage to biosamples and maximize tissue penetration depth, which is preferable for imaging of Zn^{2+} in tissues. Fresh hippocampal tissue slices were collected from 3-week-old mice I/R model. As shown in Fig. 5, the fresh hippocampal tissue slices were divided into three groups: control, HNO stimulation (group a), and Zn^{2+} stimulation (group b). The bioimaging was performed in these slices after incubated with **CHP-H** (1 μM, green channel) for 20 min, **Cyto-JN** (5 μM, red channel) for 20 min, and DAPI (100 ng/mL, blue channel) for 30 min. As displayed in group a, the strong fluorescence emission in green and red channels demonstrated that the HNO-stimulation would trigger the release of free Zn^{2+} in mice hippocampus I/R model. However, the red channel in group b was non-fluorescent indicating that Zn^{2+} could not modulate HNO generation. To assess the tissue penetration capability of the two-photon probe **CHP-H**, we reconstructed the three-dimensional (3D) image from the 100 μm tissue slices in group a (Fig. 5b). As illustrated in Fig. 5c and d, the z-stack imaging for hippocampus at a depth interval of 10 μm offered the imaging details at various confocal plains in different channels and displayed the deep tissue penetration property of the probe **CHP-H**. The above results verified that our probe **CHP-H** was able to be utilized to track the changes of Zn^{2+} concentration in mice hippocampus and was capable of performing bioimaging by penetrating the deep tissues. These bioimaging outcomes further elucidated the positive regulatory effects of HNO toward Zn^{2+}, but without reversed modulation of free Zn^{2+} toward HNO during the mice hippocampus I/R process.

4. Conclusions

In summary, we develop two-photon fluorescent probes **CHP-H** and **CHP-CH_3** for detecting intracellular Zn^{2+} changes under the regulation of HNO in cells and in mice ischemia/reperfusion models. The probes exhibit selective and sensitive behaviors toward Zn^{2+} within 60 s and possess favorable biocompatibility. With the cooperation of the HNO probe **Cyto-JN**, the bioimaging results of **CHP-H** in different living cell lines reveal that the intracellular Zn^{2+} pool could release free Zn^{2+} under the stimulation of exogenous HNO. Taking advantage of the cell I/R models, we firstly proved that cell apoptosis has positive correlation with the intracellular level of free Zn^{2+} and the HNO-induced Zn^{2+} increase can directly aggravate apoptosis process. Moreover, the bioimaging of Zn^{2+} in mice hippocampus I/R models offers the deep penetration capability of the two-photon probe **CHP-H** in tissues. All the experimental outcomes clearly demonstrate that our probes have great potential to serve as powerful chemical tools for real-time tracking of Zn^{2+} fluctuations in diagnostics of neurological diseases.

Declaration of Competing Interest

The authors declare that they have no known competing financial interests or personal relationships that could have appeared to influence the work reported in this paper.

Acknowledgements

This work was supported by Key Research and Development Project of Hainan Province (Grant. ZDYF2019130), Higher Education Research

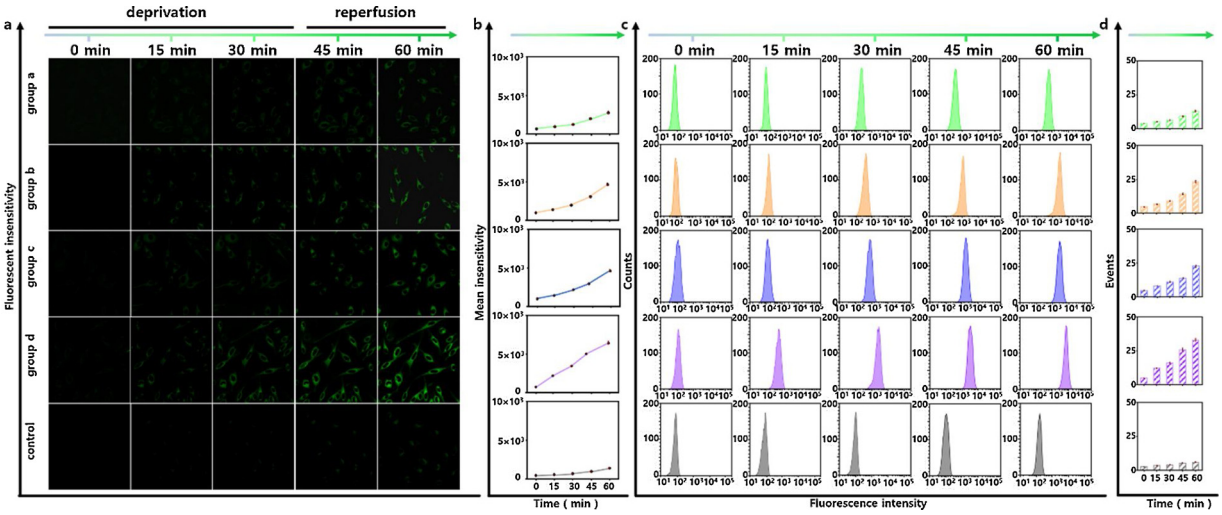

Fig. 4. Confocal microscopy imaging and flow cytometry assay of Zn^{2+} under HNO stimulation during cell I/R process. All the HT22 cells were incubated with **CHP-H** (1 μM) for 5 min then washed with fresh cell culture medium to remove excess probes and Angeli's Salt from solution. a) Confocal microscopy images of Zn^{2+} at deprivation time points at 0, 15, and 30 min. At the time point 0 min, 1 mM Angeli's Salt was added. HNO-regulation of five groups: group a, glucose deprivation; group b, serum deprivation; group c, oxygen deprivation; group d, glucose-serum-oxygen deprivation; control group. All the deprivation operations were subsequently recovered to normal culture conditions, reperfusion time points at 45, and 60 min. Fluorescence collection windows: λ_{ex} = 880 nm, λ_{em} = 520–560 nm. Scale bars: 20 μm. b) The mean intensities of the imaging results in a). c) The results of flow cytometry analysis in a). d) Mean value of flow cytometry analysis in c). The data were shown as mean (± s.d.).

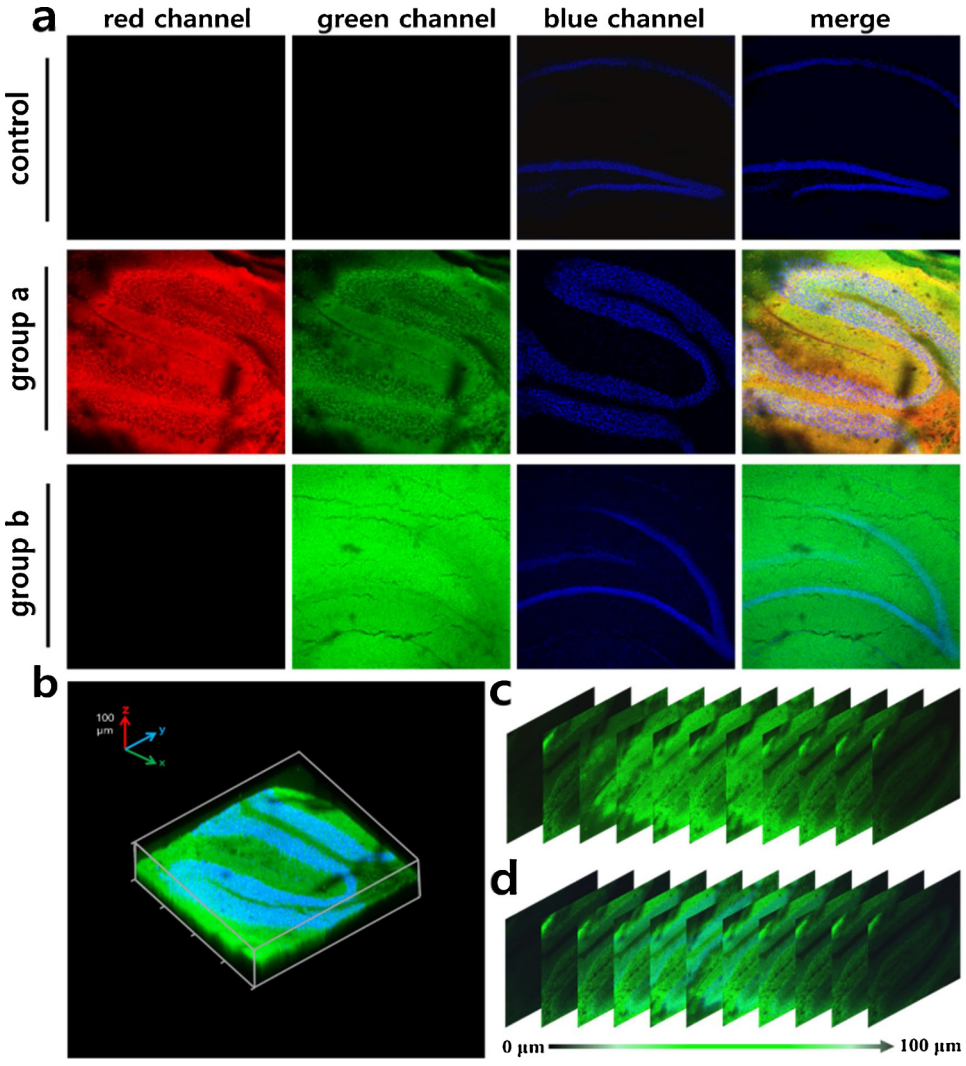

Fig. 5. Fluorescence imaging of brain hippocampus slices obtained from mice I/R models. The isolated hippocampus was from 3-week-old mice. The brain was embedded cryogenic cryopreservation and skived into 100 μm-thickness slices using a vibration slicer. Control: the slices were incubated with **CHP-H** (1 μM) for 20 min, **Cyto-JN** (5 μM) for 20 min, and DAPI (100 ng/mL) for 30 min in ACSF. Group a: the slice was treated with Angeli's Salt (1 mM) for 3 h in artificial cerebrospinal fluid (ACSF), washed three times with ACSF, then further incubated as described in control. Group b: the slice was pretreated with Zn^{2+} (25 μM) for 3 h and then treat as described in group a. a) Fluorescence imaging of hippocampus with probe **CHP-H** (1 μM), **Cyto-JN** (5 μM), and nucleus dye DAPI (100 ng/ml). And the overlay images showed the merge of red, green and blue channels. b) The three-dimensional (3D) reconstructed image of group a in green and blue channels. c) and d) The z-direction sequential images of hippocampus slice at a depth interval of 10 μm in green and green-blue channels. Fluorescence intensities collected in emission windows: Red channel (**Cyto-JN**) λ_{ex} =680 nm, λ_{em} = 690–720 nm; green channel (**CHP-H**) λ_{ex} =880 nm, λ_{em} = 510–550 nm; blue channel (DAPI) λ_{ex} =405 nm, λ_{em} =.425–500 nm. (For interpretation of the references to colour in this figure legend, the reader is referred to the web version of this article.)

Project of Hainan Province (Nos. Hnky2019ZD-29, Hnky2019ZD-30), National Natural Science Foundation of China (Nos. 21775162, 21904030), Talent Program of Hainan Medical University (XRC180006, XRC190017), Research Unit of Island Emergency Medicine, Chinese Academy of Medical Sciences (Grant. 2019RU013), and Hundred-Talent Program of Hainan (2018).

Appendix A. Supplementary data

Supplementary material related to this article can be found, in the online version, at doi:https://doi.org/10.1016/j.snb.2020.127772.

References

[1] B.L. Vallee, D.S. Auld, Zinc: biological functions and coordination motifs, Acc. Chem. Res. 26 (1993) 543–551.
[2] C.J. Frederickson, J. Koh, A.I. Bush, The neurobiology of zinc in health and disease, Nat. Rev. Neurosci. 6 (2005) 449–462.
[3] K. Kikuchi, Design, synthesis and biological application of chemical probes for bio-imaging, Chem. Soc. Rev. 39 (2010) 2048–2053.
[4] K.D. Kroncke, K. Fehsel, T. Schmidt, F.T. Zenke, I. Dasting, J.R. Wesener, H. Bettermann, K.D. Breunig, V. Kolbbachofen, Nitric oxide destroys zinc-sulfur clusters inducing zinc release from metallothionein and inhibition of the zinc finger-type yeast transcription activator LAC9, Biochem. Biophy. Res. Commun. 200 (1994) 1105–1110.
[5] W. Lin, D. Buccella, S.J. Lippard, Visualization of peroxynitrite-induced changes of labile Zn^{2+} in the endoplasmic reticulum with benzoresorufin-based fluorescent probes, J. Am. Chem. Soc. 135 (2013) 13512–13520.
[6] C. Choe, J. Lewerenz, G. Fischer, T.F. Uliasz, M.G. Espey, F.C. Hummel, S.B. King, E. Schwedhelm, R.H. Böger, C. Gerloff, Nitroxyl exacerbates ischemic cerebral injury and oxidative neurotoxicity, J. Neurochem. 110 (2009) 1766–1773.
[7] A.T. Wrobel, T.C. Johnstone, A. Deliz Liang, S.J. Lippard, P. Rivera-Fuentes, A fast and selective near-infrared fluorescent sensor for multicolor imaging of biological nitroxyl (HNO), J. Am. Chem. Soc. 136 (2014) 4697–4705.
[8] J.F. Zhang, Y. Zhou, J. Yoon, J.S. Kim, Recent progress in fluorescent and colorimetric chemosensors for detection of precious metal ions (silver, gold and platinum ions), Chem. Soc. Rev. 40 (2011) 3416–3429.
[9] S.A. Garwin, M.S. Kelley, A.C. Sue, E.L. Que, G.C. Schatz, T.K. Woodruff, T.V. O'Halloran, Interrogating intracellular zinc chemistry with a long stokes shift zinc probe ZincBY-4, J. Am. Chem. Soc. (2019) 16696–16705.
[10] Z. Xu, J. Yoon, D.R. Spring, Fluorescent chemosensors for Zn^{2+}, Chem. Soc. Rev. 39 (2010) 1996–2006.
[11] H.M. Kim, B.R. Cho, Small-molecule two-photon probes for bioimaging applications, Chem. Rev. 115 (2015) 5014–5055.
[12] A. Jiang, G. Chen, J. Xu, Y. Liu, G. Zhao, Z. Liu, T. Chen, Y. Li, T.D. James, Radiometric two-photon fluorescent probe for in situ imaging of carboxylesterase (CE)-mediated mitochondrial acidification during medication, Chem. Commun. 55 (2019) 11358–11361.
[13] H.M. Kim, M.S. Seo, M.J. An, J.H. Hong, Y.S. Tian, J.H. Choi, O. Kwon, K.J. Lee, B.R. Cho, Two-photon fluorescent probes for intracellular free zinc ions in living tissue, Angew. Chem. Int. Ed. 47 (2008) 5167–5170.
[14] P. Liu, X. Jing, F. Yu, C. Lv, L. Chen, A near-infrared fluorescent probe for the selective detection of HNO in living cells and in vivo, Analyst 140 (2015) 4576–4583.
[15] L. Yuan, W. Lin, J. Song, Y. Yang, Development of an ICT-based radiometric fluorescent hypochlorite probe suitable for living cell imaging, Chem. Commun. 47 (2011) 12691–12693.
[16] J. Guo, S.P. Duckles, J.H. Weiss, X. Li, D.N. Krause, 17b-Estradiol prevents cell death and mitochondrial dysfunction by an estrogen receptor-dependent mechanism in astrocytes after oxygen-glucose deprivation/reperfusion, Free Radic. Biol. Med. 52 (2012) 2151–2160.
[17] Y. Kitamura, Y. Iida, J. Abe, M. Mifune, F. Kasuya, M. Ohta, K. Igarashi, Y. Saito, H. Saji, In vivo measurement of presynaptic Zn2+ release during forebrain ischemia in rats, Biol. Pharm. Bull. 29 (2006) 821–823.
[18] L.M. Hyman, K.J. Franz, Probing oxidative stress: Small molecule fluorescent sensors of metal ions, reactive oxygen species, and thiols, Coord. Chem. Rev. 256 (2012) 2333–2356.
[19] J. Chan, S.C. Dodani, C.J. Chang, Reaction-based small-molecule fluorescent probes for chemoselective bioimaging, Nat. Chem. 4 (2012) 973–984.
[20] W. Chyan, D.Y. Zhang, S.J. Lippard, R.J. Radford, Reaction-based fluorescent sensor for investigating mobile Zn^{2+} in mitochondria of healthy versus cancerous prostate cells, PNAS 111 (2013) 143–148.
[21] H. Guo, G. Chen, M. Gao, R. Wang, Y. Liu, F. Yu, Imaging of endogenous hydrogen peroxide during the process of cell mitosis and mouse brain development with a near-infrared ratiometric fluorescent probe, Anal. Chem. 91 (2019) 1203–1210.
[22] X. Han, R. Wang, X. Song, F. Yu, C. Lv, L. Chen, A mitochondrial-targeting near-infrared fluorescent probe for bioimaging and evaluating endogenous superoxide anion changes during ischemia/reperfusion injury, Biomaterials 156 (2018) 134–146.
[23] X. Han, F. Yu, X. Song, L. Chen, Quantification of cysteine hydropersulfide with a ratiometric near-infrared fluorescent probe based on selenium–sulfur exchange reaction, Chem. Sci. 7 (2016) 5098–5107.
[24] X. Han, X. Song, F. Yu, L. Chen, A ratiometric near-infrared fluorescent probe for quantification and evaluation of selenocysteine-protective effects in acute inflammation, Adv. Funct. Mater. 27 (2017) 1700769.
[25] Y. Song, G. Chen, X. Han, J. You, F. Yu, A highly sensitive near-infrared ratiometric fluorescent probe for imaging of mitochondrial hydrazine in cells and in mice models, Sens. Actuators B Chem. 286 (2019) 69–76.
[26] K. Dou, G. Chen, F. Yu, Y. Liu, Z. Cao, G. Li, X. Zhao, L. Xia, L. Chen, H. Wang, J. You, A novel dual-ratiometric-response fluorescent probe for SO_2/ClO^- detection in cells and in vivo and its application in exploring the dichotomous role of SO_2 under the ClO^- induced oxidative stress, Biomaterials 133 (2017) 82–93.
[27] G. Chen, W. Zhou, C. Zhao, Y. Liu, T. Chen, Y. Li, B. Tang, Rationally optimized fluorescent probe for imaging mitochondrial SO_2 in HeLa cells and zebrafish, Anal. Chem. 90 (2018) 12442–12448.
[28] T.M. Pereira, D.P. Franco, F. Vitorio, A.E. Kummerle, Coumarin compounds in medicinal chemistry: some important examples from the last years, Curr. Topics Med. Chem. 18 (2018) 124–148.
[29] P. Jiang, Z. Guo, Fluorescent detection of zinc in biological systems: recent development on the design of chemosensors and biosensors, Coord. Chem. Rev. 248 (2004) 205–229.
[30] J.S. Wu, W.M. Liu, X.Q. Zhuang, F. Wang, P.-F. Wang, S.-L. Tao, X.-H. Zhang, S.-K. Wu, S.-T. Lee, Fluorescence turn on of coumarin derivatives by metal cations: a new signaling mechanism based on C=N isomerization, Org. Lett. 9 (2007) 33–36.
[31] Y. Zhou, H.N. Kim, J. Yoon, A selective 'off–on' fluorescent sensor for Zn^{2+} based on hydrazone–pyrene derivative and its application for imaging of intracellular Zn^{2+}, Bioorg. Med. Chem. Lett. 20 (2010) 125–128.
[32] H. Li, S. Gao, Z. Xi, A colorimetric and "turn-on" fluorescent chemosensor for Zn (II) based on coumarin Shiff-base derivative, Inorg. Chem. Commun. 12 (2009) 300–303.
[33] X. Song, X. Han, F. Yu, J. Zhang, L. Chen, C. Lv, A reversible fluorescent probe based on C=N isomerization for the selective detection of formaldehyde in living cells and in vivo, Analyst 143 (2018) 429–439.
[34] J. Wu, W. Liu, J. Ge, H. Zhang, P. Wang, New sensing mechanisms for design of fluorescent chemosensors emerging in recent years, Chem. Soc. Rev. 40 (2011) 3483–3495.
[35] J. Wan, W. Zhang, H. Guo, J. Liang, D. Huang, H. Xiao, Two spirobifluorene-based fluorescent probes with aggregation-induced emission properties: Synthesis and application in the detection of Zn2+ and cell imaging, J. Mater. Chem. C 7 (2019) 2240–2249.
[36] G.-J. Zhao, K.-L. Han, Hydrogen bonding in the electronic excited state, Acc. Chem. Res. 45 (2011) 404–413.
[37] J. Shin, P. Verwilst, H. Choi, S. Kang, J. Han, N.H. Kim, J.G. Choi, M.S. Oh, J.S. Hwang, D. Kim, Harnessing intramolecular rotation to enhance two-photon imaging of Aβ plaques through minimizing background fluorescence, Angew. Chem. Int. Ed. 131 (2019) 5704–5708.
[38] D. Cao, Z. Liu, P. Verwilst, S. Koo, P. Jangjili, J.S. Kim, W. Lin, Coumarin-based small-molecule fluorescent chemosensors, Chem. Rev. 119 (2019) 10403–10519.
[39] P. Job, Job's method of continuous variation, Ann. Chim. 9 (1928) 113–203.
[40] H.A. Benesi, J. Hildebrand, A spectrophotometric investigation of the interaction of iodine with aromatic hydrocarbons, J. Am. Chem. Soc. 71 (1949) 2703–2707.
[41] C. Xu, W.W. Webb, Measurement of two-photon excitation cross sections of molecular fluorophores with data from 690 to 1050 nm, J. Opt. Soc. Am. B 13 (1996) 481–491.
[42] R.A. Colvin, W.R. Holmes, C.P. Fontaine, W. Maret, Cytosolic zinc buffering and muffling: their role in intracellular zinc homeostasis, Metallomics 2 (2010) 306–317.
[43] P. Rivera-Fuentes, A.T. Wrobel, M.L. Zastrow, M. Khan, J. Georgiou, T.T. Luyben, J.C. Roder, K. Okamoto, S.J. Lippard, A far-red emitting probe for unambiguous detection of mobile zinc in acidic vesicles and deep tissue, Chem. Sci. 6 (2015) 1944–1948.

Mingshun Li is a Master student of Qufu Normal University. His research focuses on the design and synthesis of small molecule fluorescent probes for detecting intracellular biopsies.

Professor Yanlong Xing received her Ph.D. degree from the Technical University of Berlin (TU Berlin), Germany in 2017. After her postdoctoral research in the Leibniz Institute of Analytical Science (ISAS Berlin), she joined the Hainan Medical University as a professor in August 2018. Her current research interests focus on extracellular vesicle-based liquid biopsy, microfluidic technology and the development of functional materials for biosensors.

Yuxia Zou is a Master student of Hainan Medical University. Her research focuses on the design and synthesis of small molecule fluorescent probes for surgery-guide in cancer.

Professor Guang Chen has graduated with his Ph.D. from the Northwest Plateau Institute of Biology of Chinese Academy of Sciences, and now is a professor in Qufu Normal university. His research interests focus on the design of organic probes, the exploring of sensing mechanism, the pretreatment techniques of derivatization.

Professor Jinmao You a scholar of CAS Hundred (No. 328) is now the directors of both the key laboratory of life-organic analysis and the Key Laboratory of Pharmaceutical Intermediates and Analysis of Natural Medicine, Qufu Normal University. He has obtained some achievements in the fields of derivatization techniques used for the component's analysis of biological and environmental samples.

Professor Fabiao Yu received his Ph.D. degree from Dalian University of Technology and Dalian Institute of Chemical Physics, Chinese Academy of Sciences in 2013. After four years' work at Yantai Institute of Coastal Zone Research, Chinese Academy of Sciences as an associate professor, he joined Hainan Medical University from October 2018 as a full professor. His research interests focus on molecular imaging, theranostics and organic functional materials.